Science
AAAS

Ultrahigh Porosity in Metal-Organic Frameworks
Hiroyasu Furukawa, *et al.*
Science **329**, 424 (2010);
DOI: 10.1126/science.1192160

Science (print ISSN 0036-8075; online ISSN 1095-9203) is published weekly, except the last week in December, by the American Association for the Advancement of Science, 1200 New York Avenue NW, Washington, DC 20005.

locations (~6300 km on a great circle) imply that such environments have multiple occurrences in Noachian terrain. The high carbonate concentration in the Comanche outcrops is evidence for climate models (*3*) involving a CO_2 greenhouse gas on a wet and warm early Mars and subsequent sequestering of at least part of that atmosphere in carbonate minerals.

References and Notes

1. J. L. Gooding, *Icarus* **33**, 483 (1978).
2. J. L. Gooding, in *The Solar System: Observations and Interpretations, Rubey Volume IV*, M. G. Kivelson, Ed. (Prentice Hall, Upper Saddle River, NJ, 1986), pp. 208–229.
3. J. B. Pollack, J. F. Kasting, S. M. Richardson, K. Poliakoff, *Icarus* **71**, 203 (1987).
4. D. C. Catling, *J. Geophys. Res.* **104**, 16453 (1999).
5. J. C. Bridges *et al.*, *Space Sci. Rev.* **96**, 365 (2001).
6. B. L. Ehlmann *et al.*, *Science* **322**, 1828 (2008).
7. J. L. Bandfield, T. D. Glotch, P. R. Christensen, *Science* **301**, 1084 (2003).
8. M. D. Lane, M. D. Dyar, J. L. Bishop, *Geophys. Res. Lett.* **31**, L19702 (2004).
9. V. E. Hamilton, H. Y. McSween Jr., B. Hapke, *J. Geophys. Res.* **110**, E12006 (2005).
10. W. V. Boynton *et al.*, *Science* **325**, 61 (2009).
11. M. P. Golombek *et al.*, *J. Geophys. Res.* **111**, (E2), E02S07 (2006).
12. R. V. Morris *et al.*, *J. Geophys. Res.* **111**, E02S13 (2006).
13. S. W. Squyres *et al.*, *J. Geophys. Res.* **111**, E02S11 (2006).
14. D. W. Ming *et al.*, *J. Geophys. Res.* **111**, E02S12 (2006).
15. T. J. McCoy *et al.*, *J. Geophys. Res.* **113**, E06S03 (2008).
16. R. E. Arvidson *et al.*, *J. Geophys. Res.* **113**, E12S33 (2008).
17. S. W. Squyres *et al.*, *Science* **316**, 738 (2007).
18. S. W. Squyres *et al.*, *Science* **320**, 1063 (2008).
19. R. V. Morris *et al.*, *J. Geophys. Res.* **113**, E12S42 (2008).
20. A. S. Yen *et al.*, *J. Geophys. Res.* **113**, E06S10 (2008).
21. D. W. Ming *et al.*, *J. Geophys. Res.* **113**, E12S39 (2008).
22. G. Klingelhöfer *et al.*, *J. Geophys. Res.* **108**, 8067 (2003).
23. Supporting material available on *Science* Online includes laboratory studies, spectral unmixing of Mini-TES spectra, and Pancam multispectral spectroscopy.
24. R. Rieder *et al.*, *J. Geophys. Res.* **108**, 8066 (2003).
25. J. L. Campbell *et al.*, *J. Geophys. Res.* **113**, E06S11 (2008).
26. P. R. Christensen *et al.*, *J. Geophys. Res.* **108**, 8064 (2003).
27. M. S. Ramsey, P. R. Christensen, *J. Geophys. Res.* **103**, 577 (1998).
28. D. W. Mittlefehldt, *Meteoritics* **29**, 214 (1994).
29. A. H. Treiman, *Meteoritics* **30**, 294 (1995).
30. R. P. Harvey, H. Y. McSween Jr., *Nature* **382**, 49 (1996).
31. S. J. Gaffey, *J. Geophys. Res.* **92**, 1429 (1987).
32. T. M. Hoefen *et al.*, *Science* **302**, 627 (2003).
33. V. E. Hamilton, P. R. Christensen, *Geology* **33**, 433 (2005).
34. T. Usui, H. Y. McSween Jr., B. C. Clark III, *J. Geophys. Res.* **113**, E12S44 (2008).
35. D. C. Golden *et al.*, *Meteorit. Planet. Sci.* **35**, 457 (2000).
36. A. H. Treiman *et al.*, *Earth Planet. Sci. Lett.* **204**, 323 (2002).
37. A. Steele *et al.*, *Meteorit. Planet. Sci.* **42**, 1549 (2007).
38. L. E. Borg *et al.*, *Science* **286**, 90 (1999).
39. D. Banks *et al.*, *Geothermics* **28**, 713 (1999).
40. H. E. F. Amundsen, W. L. Griffin, S. Y. O'Reilly, *Tectonophysics* **139**, 169 (1987).

41. R.V.M. and D.W.M. acknowledge the NASA Johnson Space Center and the NASA Mars Exploration Program for support. R.V.M. acknowledges the NASA Ames Astrobiology Institute for support. S.W.R. acknowledges the NASA Mars Data Analysis Program for support. G.K. and I.F. acknowledge support by the German Space Agency DLR under contract 50QM9902. A portion of the research described in this paper was carried out at the Jet Propulsion Laboratory, California Institute of Technology, under a contract with NASA. We thank P. B. Niles for carbonate samples, L. Le for carbonate microprobe analyses, and J. L. Campbell for calculation of excess light-element concentrations from APXS data.

Supporting Online Material

www.sciencemag.org/cgi/content/full/science.1189667/DC1
SOM Text
Figs. S1 and S2
Tables S1 and S2
References

16 March 2010; accepted 24 May 2010
Published online 3 June 2010;
10.1126/science.1189667
Include this information when citing this paper.

Ultrahigh Porosity in Metal-Organic Frameworks

Hiroyasu Furukawa,[1] Nakeun Ko,[2] Yong Bok Go,[1] Naoki Aratani,[1] Sang Beom Choi,[2] Eunwoo Choi,[1] A. Özgür Yazaydin,[3] Randall Q. Snurr,[3] Michael O'Keeffe,[1] Jaheon Kim,[2]* Omar M. Yaghi[1,4]*

Crystalline solids with extended non-interpenetrating three-dimensional crystal structures were synthesized that support well-defined pores with internal diameters of up to 48 angstroms. The $Zn_4O(CO_2)_6$ unit was joined with either one or two kinds of organic link, 4,4′,4″-[benzene-1,3,5-triyl-tris (ethyne-2,1-diyl)]tribenzoate (BTE), 4,4′,44″-[benzene-1,3,5-triyl-tris(benzene-4,1-diyl)]tribenzoate (BBC), 4,4′,44″-benzene-1,3,5-triyl-tribenzoate (BTB)/2,6-naphthalenedicarboxylate (NDC), and BTE/biphenyl-4,4′-dicarboxylate (BPDC), to give four metal-organic frameworks (MOFs), MOF-180, -200, -205, and -210, respectively. Members of this series of MOFs show exceptional porosities and gas (hydrogen, methane, and carbon dioxide) uptake capacities. For example, MOF-210 has Brunauer-Emmett-Teller and Langmuir surface areas of 6240 and 10,400 square meters per gram, respectively, and a total carbon dioxide storage capacity of 2870 milligrams per gram. The volume-specific internal surface area of MOF-210 (2060 square meters per cubic centimeter) is equivalent to the outer surface of nanoparticles (3-nanometer cubes) and near the ultimate adsorption limit for solid materials.

One of the most important properties of metal-organic frameworks (MOFs) is their high porosity (fraction of void volume to total volume) and high specific surface area, which has led to many applications concerned with gas storage, separations, and catalysis (*1*–*6*). An important consideration in maximizing the uptake of gases within porous MOF crystals is to increase the number of adsorptive sites within a given material. The simplest way to accomplish this is to use slim organic linkers in which the faces and edges of the constituent units (such as phenylene rings) are exposed for gas adsorption (*7*, *8*). Thus in principle, expansion of the organic links should lead to MOFs with ultrahigh porosity.

However, difficulties arise when targeting such MOFs: (i) Expanded links often yield fragile frameworks (*9*), and (ii) the large void space within the crystal framework makes it generally susceptible to self-interpenetration (two lattices grow and interpenetrate each other), precluding high porosity (*10*, *11*). In this report, we present four examples of MOFs for which it was possible to overcome the two challenges and to obtain materials with the highest porosity yet achieved. Specifically, the synthesis and crystal structures of the four MOFs (MOF-180, -200, -205, and -210) are described, three of which show exceptional porosity. In particular, MOF-210 exhibits the highest BET (Brunauer-Emmett-Teller) and Langmuir surface area (6240 and 10,400 $m^2\ g^{-1}$) and pore volume (3.60 $cm^3\ g^{-1}$ and 0.89 $cm^3\ cm^{-3}$ of MOF crystal) yet reported.

In the pursuit of MOFs with ultrahigh porosity, the octahedral $Zn_4O(CO_2)_6$ has had a prominent role as a building unit in producing structures exhibiting exceptional porosity (Scheme 1) (*7*, *8*, *12*–*14*). Joining such units by 4,4′,44″-benzene-1,3,5-triyl-tribenzoate (BTB) and/or 1,4-benzenedicarboxylate (BDC) linkers produces MOF-5, UMCM-2, and MOF-177 (*7*, *8*, *12*–*14*), which heretofore showed the highest BET surface area and pore volume among MOFs (Table 1). We sought to test the likelihood of reaching higher porosities by expanding the links in MOF-177 and by further exploring the role of mixed links in producing the desired structures. We prepared the expanded forms of MOF-177 from 4,4′,4″-[benzene-1,3,5-triyl-tris(ethyne-2,1-diyl)]tribenzoate (BTE) and 4,4′,4″-[benzene-1,3,5-triyl-tris(benzene-4,1-diyl)] tribenzoate (BBC) to give MOF-180 and MOF-200, respectively, and used mixed 4,4′,4″-benzene-1,3,5-

[1]Center for Reticular Chemistry at the California NanoSystems Institute, and Department of Chemistry and Biochemistry, University of California Los Angeles (UCLA), 607 Charles E. Young Drive East, Los Angeles, CA 90095, USA. [2]Department of Chemistry, Soongsil University, Seoul 156-743, Korea. [3]Department of Chemical and Biological Engineering, Northwestern University, Evanston, IL 60208, USA. [4]UCLA–Department of Energy (DOE) Institute of Genomics and Proteomics, UCLA, 607 Charles E. Young Drive East, Los Angeles, CA 90095, USA.

*To whom correspondence should be addressed. E-mail: jaheon@ssu.ac.kr (J.K.); yaghi@chem.ucla.edu (O.M.Y.)

triyl-tribenzoate (BTB)/2,6-naphthalenedicarboxylate (NDC) and BTE/biphenyl-4,4′-dicarboxylate (BPDC) links to obtain MOF-205 and 210 (Scheme 1 and Table 1). Here, we present the synthesis and crystal structures of the four MOFs and report their adsorption of nitrogen (77 K, 1 bar), hydrogen (77 K, 80 bar), and methane and carbon dioxide (298 K, 80 and 55 bar, respectively).

Scheme 1. $Zn_4O(CO_2)_6$ unit (left) is connected with organic linkers (middle) to form MOFs.

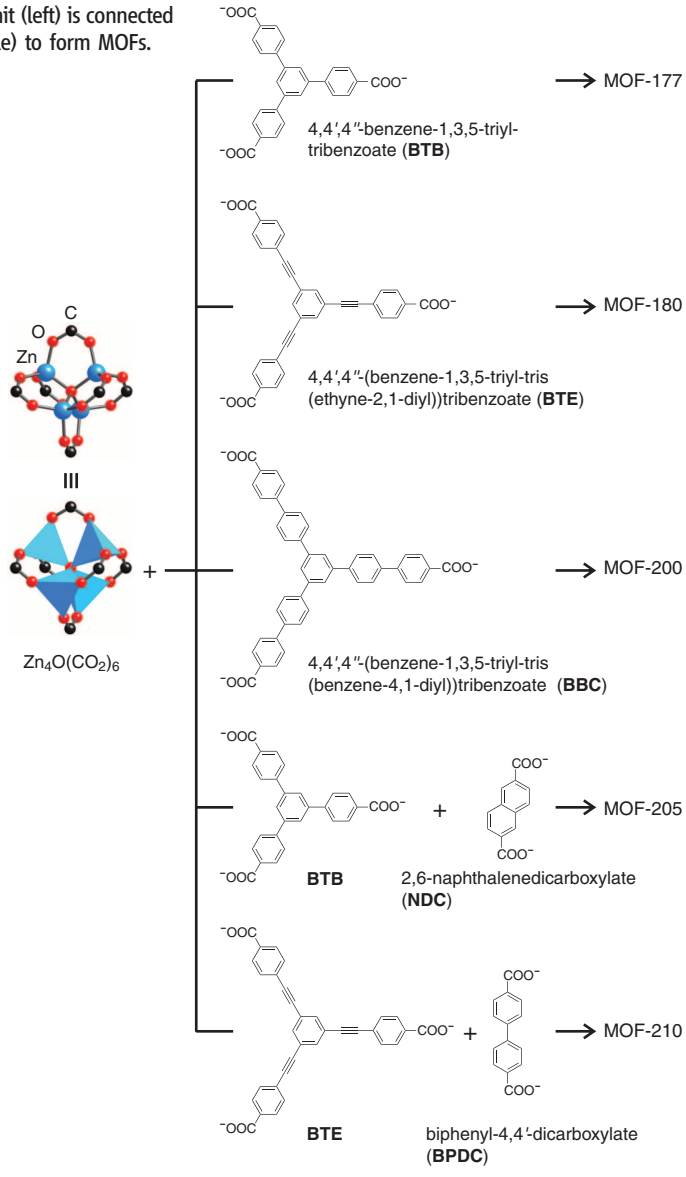

Table 1. Porosity data of highly porous MOFs. A_{BET}, A_{Lang}, and A_{geo} are the BET, Langmuir, and geometric surface areas, respectively. V_p is the measured pore volume. ND, no data; H_2T2DC, thieno [3,2-*b*]thiophene-2,5-dicarboxylic acid.

Compound	RCSR code	Linker	Void volume (%)	Crystal density (g cm^{-3})	A_{BET} (m^2 g^{-1})	A_{Lang} (m^2 g^{-1})	A_{geo}* (m^2 g^{-1})	V_p (cm^3 g^{-1})	Reference
MOF-5	**pcu**	BDC	79	0.59	3800	4400	3390	1.55	(*14*)
MOF-177	**qom**	BTB	83	0.43	4500	5340	4740	1.89	(*22*)
MOF-180	**qom**	BTE	89	0.25	ND	ND	6080	ND	This work
MOF-200	**qom**	BBC	90	0.22	4530	10400	6400	3.59	This work
MOF-205	**ith-d**	BTB,NDC	85	0.38	4460	6170	4680	2.16	This work
MOF-210	**toz**	BTE,BPDC	89	0.25	6240	10400	5850	3.60	This work
UMCM-2	**umt**	BTB,T2DC	83	0.40	5200	6060	4360	2.32	(*13*)
MIL-101c	**mtn-e**	BDC	83	0.44	4230	5900	2880	2.15	(*23*, *24*)

*See section S6 in (*17*).

It is a basic tenet of reticular chemistry that, in the assembly of variously shaped geometric units, frameworks with highly symmetric vertices and, ideally, one kind of link ("edge transitive") would be most likely to form. In the present case of linking octahedral and triangular units, at first sight the most favorable net ("net" refers to the periodic graph that is the underlying topology of the structure) appears to be **pyr** (*15*). Indeed, that is the observed net in MOF-150 (*16*) and related MOFs; however, these form unwanted (denser) structures with two interpenetrating networks. This is unsurprising because **pyr** is a net with a self-dual tiling (the same net from when linkers replace vertices, and vice versa). The interpenetrating dual nets have the same connectivity involving alternating octahedra and triangles (Fig. 1, A and B). We recognized that it is necessary to build a MOF with expanded organic links that is based on a net with a very different from its dual so as to avoid interpenetrating frameworks (Fig. 1, C and D) (*7*).

In earlier studies, we found that with aromatic tritopic linkers of the sort used here a closely related net (**qom**) is produced in MOF-177 (Fig. 1F) (*7*), in which alternating octahedral $Zn_4O(CO_2)_6$ and triangular BTB units produce one of the most porous structures yet reported, and for which the interpenetrating dual net involves direct links between octahedral units and between triangular units (Fig. 1, C to E). However, it is impossible to create a MOF with such linkages, and an interpenetrating pair of MOFs does not appear.

Accordingly, an isoreticular non-interpenetrating expansion of MOF-177 was targeted by using BTE or BBC to make the highly porous materials MOF-180 and -200 (Fig. 1, G and H) (*17*). The unit cell volumes of MOF-180 and -200 are respectively 1.9 and 2.6 times greater than that of MOF-177, with void volumes of 89 and 90% of the crystal volume (Table 1). The cage sizes for MOF-180 and -200 are 15 by 23 and 18 by 28 Å, respectively, which is on the border of micropores and mesopores. The bulk density for MOF-200 is 0.22 g cm^{-3}, implying that the **qom** net is advantageous to reduce the dead space and increase the gas storage capacity per unit volume in a closed tank. This density is the lowest for MOF structures, and of any other crystals at room temperature except for those of the least dense covalent organic frameworks (*18*).

On the basis of our effective use of the **qom** net for the successful synthesis of the non-interpenetrating MOF-180 and MOF-200, we recognized that other MOFs of nets without self-dual tilings could be made if we used mixed organic links of mixed connectivity. We used both tritopic H_3BTB and ditopic H_2NDC in a reaction with Zn ions to produce $Zn_4O(CO_2)_6$ units and make MOF-205 (Fig. 2A) (*17*). Its structure belongs to a cubic space group $Pm\bar{3}n$ and consists of one type of $Zn_4O(CO_2)_6$ octahedral unit whose vertices are connected to four BTB and two NDC links [after this work was completed, the same compound was independently reported as DUT-6 (*19*)]. The topology of MOF-205 (**ith-d**) is of considerable intrinsic interest; all the rings of

the underlying net are 5-rings, and it forms a face-transitive tiling of dodecahedra [5^{12}] and tetrahedra [5^4] in the ratio 1:3 (Fig. 2C). The dual structure (**ith**) is an edge-transitive net with tetrahedral and icosahedral vertices and very different from the original net.

Attempts at isoreticular expansion of MOF-205 by use of the linkers BTE and BPDC produced a different but related material (termed MOF-210) (Fig. 2B). MOF-210 was prepared from a solvothermal reaction of H_3BTE, H_2BPDC, and zinc(II) nitrate hexahydrate (*17*). Similar to the discovery of MOF-177 (*7*), this proved to be serendipitous: Rather than the 12-face tile of **ith-d**, the new topology has 30-face tiles, and the full tiling consists of [$4^6.5^{24}$], [$4^3.5^6$], and [5^4] in the ratio 1:2:3 (Fig. 2D). It is hard to envisage how the connectivity is determined; however, we believe the subtle difference in the link length ratio (for example, 0.76 for MOF-210 and 0.79 for UMCM-2) may be important. The dimension of the largest cage in MOF-210 is 26.9 by 48.3 Å, which comprises 18 Zn_4O units with 14 BTE and 6 BPDC links. The estimated bulk density (void space) is 0.25 g cm^{-3} (89%), which is almost the same as that for MOF-180.

Considering the bulk density and void space calculated from the crystal structure analyses, MOF-200 and -210 are promising candidates to realize ultrahigh surface area. Before gas adsorption measurements, grand canonical Monte Carlo (GCMC) simulations were performed to calculate nitrogen adsorption isotherms (*17*). Predicted isotherms (Fig. 3A) show unusual steps attributed to the micropore filling at P/P_0 = 0.12 and 0.26 (for MOF-200 and -210, respectively), and total nitrogen uptakes in MOF-200 and -210 reaching 2650 and 2300 cm^3 g^{-1}, respectively. The BET and Langmuir surface areas determined from these calculated isotherms are respectively 6260 and 12,040 for MOF-200 and 6580 and 10,450 m^2 g^{-1} for MOF-210; these are much higher than values reported previously for other porous crystals.

To assess the architectural stability and porosity of these low-density MOFs, and to confirm the calculations, we measured nitrogen adsorption isotherms on the guest free samples of MOF-200, -205, and -210. Preliminary trials revealed that the solvent exchange followed by pore evacuation under vacuum was not effective to activate MOF-200 and -210 without losing the porosity. Thus, these crystals were fully exchanged with liquid CO_2, they were kept under supercritical CO_2 atmosphere, and then their pores were bled of CO_2 in order to yield activated samples (*20*, *21*). Successful guest removal was confirmed by powder x-ray diffraction measurements and elemental analyses (*21*). As shown in Fig. 3A, all MOF samples show distinctive steps (P/P_0 = 0.14, 0.09, and 0.27 for MOF-200, -205, and -210, respectively), and the profiles for MOF-200 and -210 are nearly the same as the predicted isotherms. The maximum nitrogen uptake capacities at 77 K in MOF-200, -205, and -210 are 2340, 1410, and 2330 cm^3 g^{-1}, respectively. These uptake values in MOF-200 and -210 are well beyond those observed for other crystalline porous solids (*7*, *13*, *14*, *22*–*24*). Further, the measured values are near the values predicted on the basis of the structure, indicating that these materials are well activated. Because of the successful sample activation, extremely high BET (and Langmuir) surface areas were obtained: 4530 (10,400), 4460 (6,170), and 6240 (10,400) m^2 g^{-1} for MOF-200, -205, and -210, respectively (*25*). The BET surface area of MOF-210 is the highest reported for crystalline materials. It has recently been shown that the BET method applied to nitrogen adsorption isotherms provides physically meaningful values for the surface areas of MOFs (*25*).

Given the exceptional properties of such materials, it is expected that MOFs with ultrahigh surface area would exhibit exceptional gas storage capacity. Accordingly, this series of MOFs was subjected to high-pressure hydrogen (77 K) and methane (298 K) adsorption so as to examine their potential utility in the storage of gaseous fuels (Fig. 3, B and C, and table S12). In hydrogen isotherms, these MOFs reach saturation

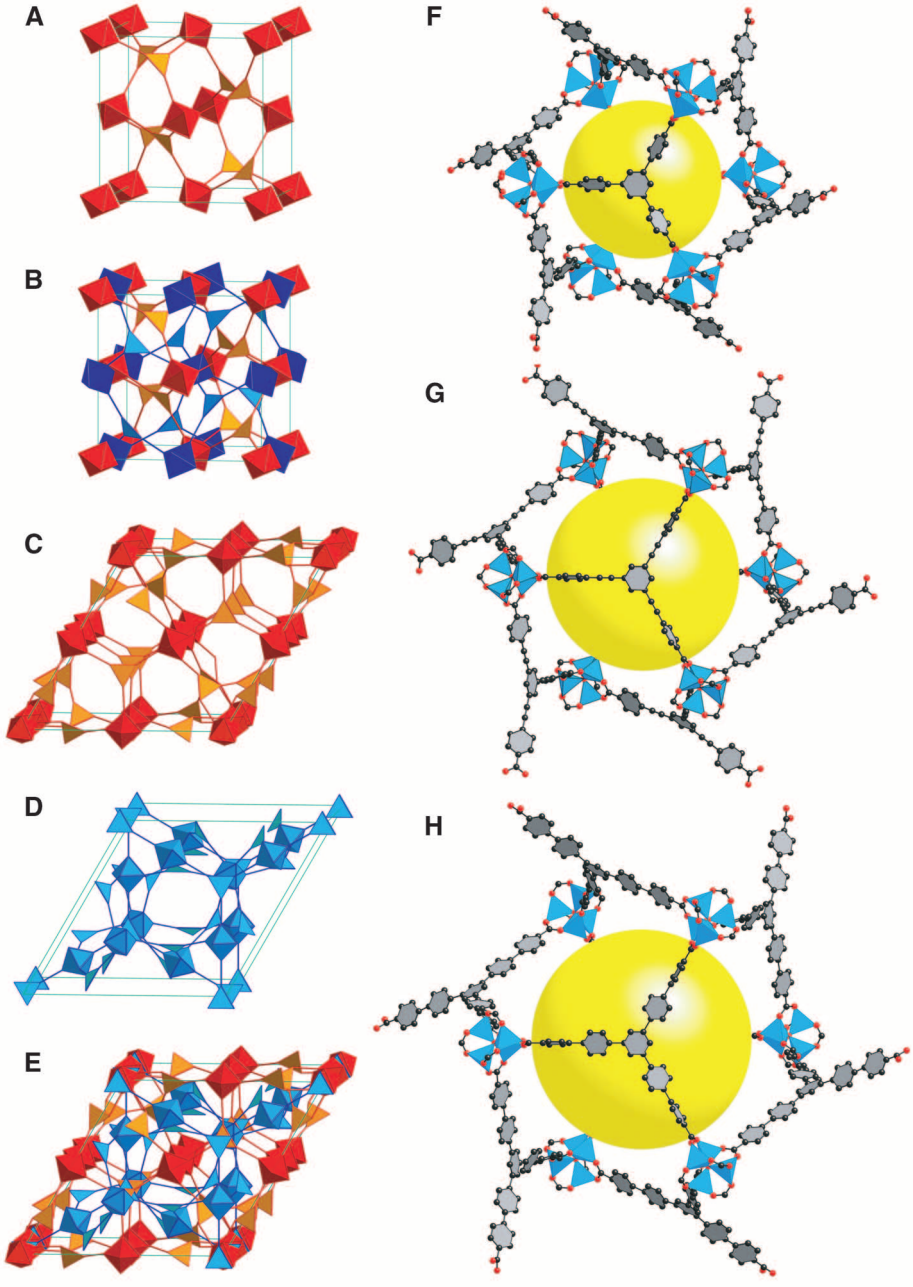

Fig. 1. Connectivity of **pyr** and **qom** (6,3)-coordinated nets. For **pyr** (**A**), pairs of **pyr** nets can naturally interpenetrate (**B**). In contrast, **qom** is not self-dual (**C** to **E**); the connectivity of the net of the dual tiling for **qom** (D) is very different from the original (C). Crystal structures of MOF-177 (**F**), MOF-180 (**G**), and MOF-200 (**H**) are found in **qom** net (C). The yellow ball is placed in the structure for clarity and to indicate space in the cage. Zn, blue, tetrahedral; O, red; and C, black. Hydrogen atoms are omitted for clarity.

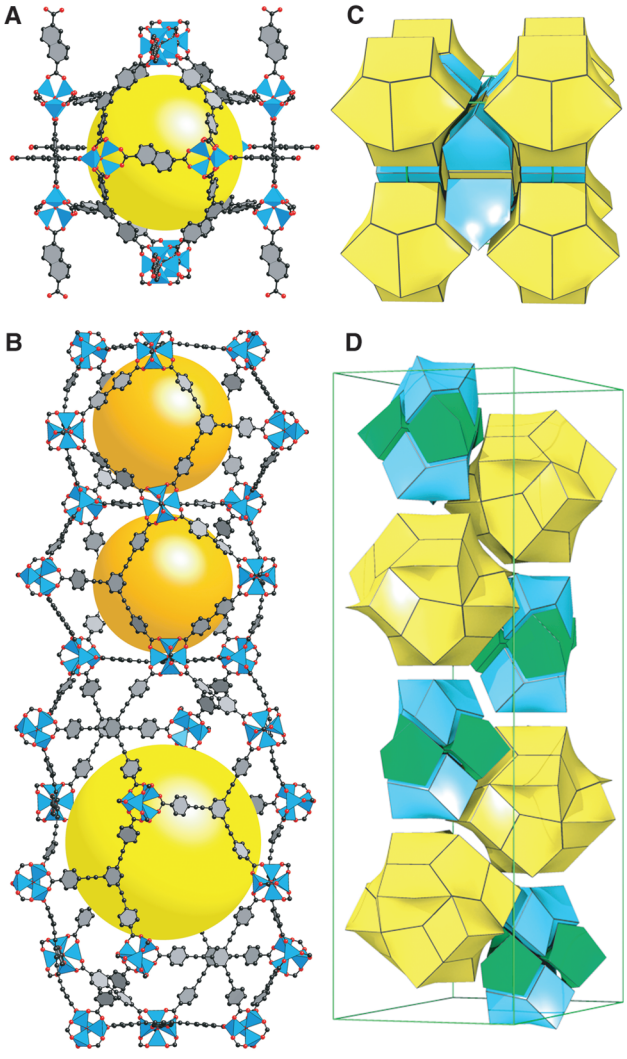

Fig. 2. Crystal structures of MOF-205 (**A**) and MOF-210 (**B**). The yellow and orange balls are placed in the structure for clarity and to indicate space in the cage. Atom colors are the same as in Fig. 1. Tiling of (**C**) **ith-d** and (**D**) **toz** nets.

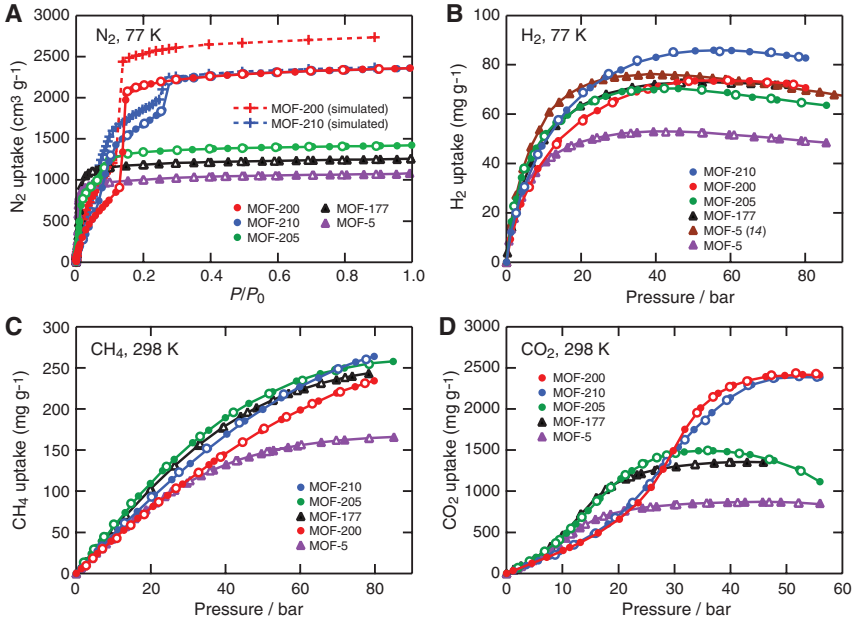

Fig. 3. (**A**) Low-pressure N_2 isotherms of MOF-5, -177, -200, -205, and -210 at 77 K. Simulated isotherms of MOF-200 and -210 were overlaid. P/P_0, relative pressure. High-pressure H_2 isotherms were measured at 77 K (**B**), and (**C**) CH_4 and (**D**) CO_2 isotherms were measured at 298 K of the same MOFs.

uptakes, and the saturation pressure increases with an increase in the cavity size. The surface excess hydrogen uptake in MOF-210 (86 mg g^{-1}) is higher than those in MOF-5, MOF-177, UMCM-2, and NOTT-112 (*13*, *14*, *22*, *26*, *27*). The total uptake that a material can store is more relevant to the practicability of using H_2 as a fuel, but it cannot be measured experimentally. Therefore, we estimated this value using the pore volume and the density of hydrogen at 77 K (*22*). The calculated gravimetric hydrogen density in MOF-210 (176 mg g^{-1}) exceeds that of typical alternative fuels (methanol and ethanol) and hydrocarbons (pentane and hexane). MOF-200 and -205 also show large total hydrogen uptake (163 and 123 mg g^{-1}, respectively); again, these values are higher than MOF-177 (*22*).

Methane uptake was measured at 298 K and up to 80 bar (Fig. 3C); under the present experimental conditions, all isotherms were not saturated. Although the excess methane uptake in MOF-200, -205, and -210 (234, 258, and 264 mg g^{-1} at 80 bar, respectively) were smaller than that in PCN-14 (253 mg g^{-1} at 290 K and 35 bar, respectively) (*28*), the calculated total uptakes (446, 394, and 476 mg g^{-1} for MOF-200, -205, and -210, respectively) were more than 50% greater than those of PCN-14. Moreover, the corresponding volumetric methane densities in the present MOFs are respectively 2, 3, and 2.5 times greater than volumetric bulk density (grams per liter) of methane at the same temperature and pressure (table S12). Because the isotherms are nearly linear up to 80 bar, these materials can deliver most of the sorbed methane in the pressure range between 10 to 200 bar.

Large storage volumes should also be desirable for short-term CO_2 storage. High-pressure CO_2 isotherms for all three MOFs were collected and are presented in Fig. 3D. These MOFs show sigmoidal isotherms, and the pressure for the steep rise reflects the pore size of the MOFs. An isotherm for MOF-205 is saturated at a pressure of 37 bar, whereas the saturation pressure for MOF-200 and -210 are ~50 bar. In contrast to hydrogen and methane uptakes, the amounts of excess CO_2 uptake are directly related to the total pore volume. The CO_2 uptake value of 2400 mg g^{-1} in both MOF-200 and -210 exceeds those of any other porous material, such as MOF-177 and MIL-101c(Cr) (1470 and 1760 mg g^{-1}, respectively) (*24*).

The ultrahigh surface areas exhibited by MOF-200 and -210 are near the ultimate limit for solid materials. To appreciate this, it is useful to note that all these compounds have a volume-specific surface area in the range of 1000 to 2000 $m^2\ cm^{-3} = 1 \times 10^9$ to $2 \times 10^9\ m^{-1}$, and for a cube of edge d the external surface area/volume is $6d^2/d^3 = 6/d$. Thus, for a monodisperse powder of cubic nanoparticles to have external surface that is equal to that of these MOFs the cube edge would have to be only 3 to 6 nm, which is a size far too small to practically realize in stable dry powders and therefore impossible to access the full surface area of such particles. This analysis

emphasizes that MOFs are truly "nanomaterials" in the sense that they can be designed to give volume-specific surface areas that are equal to the external surface areas of nanometer-sized particles.

References and Notes

1. U. Mueller *et al.*, *J. Mater. Chem.* **16**, 626 (2006).
2. S. Kitagawa, R. Kitaura, S. Noro, *Angew. Chem. Int. Ed.* **43**, 2334 (2004).
3. J. Y. Lee *et al.*, *Chem. Soc. Rev.* **38**, 1450 (2009).
4. X. Zhao *et al.*, *Science* **306**, 1012 (2004).
5. M. Dincă, J. R. Long, *Angew. Chem. Int. Ed.* **47**, 6766 (2008).
6. O. M. Yaghi *et al.*, *Nature* **423**, 705 (2003).
7. H. K. Chae *et al.*, *Nature* **427**, 523 (2004).
8. J. L. C. Rowsell, E. C. Spencer, J. Eckert, J. A. K. Howard, O. M. Yaghi, *Science* **309**, 1350 (2005).
9. J. K. Schnobrich, K. Koh, K. N. Sura, A. J. Matzger, *Langmuir* **26**, 5808 (2010).
10. B. Chen, M. Eddaoudi, S. T. Hyde, M. O'Keeffe, O. M. Yaghi, *Science* **291**, 1021 (2001).
11. X. Lin, J. Jia, P. Hubberstey, M. Schröder, N. R. Champness, *CrystEngComm* **9**, 438 (2007).
12. H. Li, M. Eddaoudi, M. O'Keeffe, O. M. Yaghi, *Nature* **402**, 276 (1999).
13. K. Koh, A. G. Wong-Foy, A. J. Matzger, *J. Am. Chem. Soc.* **131**, 4184 (2009).
14. S. S. Kaye, A. Dailly, O. M. Yaghi, J. R. Long, *J. Am. Chem. Soc.* **129**, 14176 (2007).
15. M. O'Keeffe, M. A. Peskov, S. J. Ramsden, O. M. Yaghi, *Acc. Chem. Res.* **41**, 1782 (2008).
16. H. K. Chae, J. Kim, O. D. Friedrichs, M. O'Keeffe, O. M. Yaghi, *Angew. Chem. Int. Ed.* **42**, 3907 (2003).
17. Materials and methods are available as supporting material on *Science* Online.
18. H. M. El-Kaderi *et al.*, *Science* **316**, 268 (2007).
19. N. Klein *et al.*, *Angew. Chem. Int. Ed.* **48**, 9954 (2009).
20. A. P. Nelson, O. K. Farha, K. L. Mulfort, J. T. Hupp, *J. Am. Chem. Soc.* **131**, 458 (2009).
21. C. J. Doonan, W. Morris, H. Furukawa, O. M. Yaghi, *J. Am. Chem. Soc.* **131**, 9492 (2009).
22. H. Furukawa, M. A. Miller, O. M. Yaghi, *J. Mater. Chem.* **17**, 3197 (2007).
23. G. Férey *et al.*, *Science* **309**, 2040 (2005).
24. P. L. Llewellyn *et al.*, *Langmuir* **24**, 7245 (2008).
25. K. S. Walton, R. Q. Snurr, *J. Am. Chem. Soc.* **129**, 8552 (2007).
26. A. G. Wong-Foy, A. J. Matzger, O. M. Yaghi, *J. Am. Chem. Soc.* **128**, 3494 (2006).
27. Y. Yan *et al.*, *Chem. Commun. (Camb.)* **2009**, 1025 (2009).
28. S. Ma *et al.*, *J. Am. Chem. Soc.* **130**, 1012 (2008).

29. This work is partially supported by BASF SE. The synthesis, characterization of MOF-200, and nitrogen, methane, and carbon dioxide adsorption measurements of the MOFs are supported by the DOE Office of Basic Energy Sciences (DE-FG02-08ER15935 to O.M.Y.), and hydrogen adsorption measurements are supported by the DOE (DE-FG36-05GO15001 to O.M.Y.). We thank the Hydrogen Energy R&D Center, one of the 21st Century Frontier R&D Programs (the Ministry of Education, Science and Technology of Korea to J.K.), and the Defense Threat Reduction Agency (HDTRA1-08-C-005 to R.Q.S.). We thank N. W. Ockwig (Sandia National Laboratories) for his initial work, S. Khan (UCLA) for his help in single-crystal x-ray structure collection and analysis of MOF-200, Y. K. Park and E. Jo (Soongsil University) for their synthesis work of organic links, Accelrys Korea for MS Modeling support, and Pohang Accelerator Laboratory, Korea (2009-2063-12, 2009-2063-18). Crystallographic data for the structures reported in this paper have been deposited with the Cambridge Crystallographic Data Centre under reference numbers CCDC 775690 to 775693. These data can be obtained free of charge via www.ccdc.cam.ac.uk/conts/retrieving.html (or from the Cambridge Crystallographic Data Centre, 12 Union Road, Cambridge CB2 1EZ, UK).

Supporting Online Material

www.sciencemag.org/cgi/content/full/science.1192160/DC1
Materials and Methods
Figs S1 to S39
Tables S1 to S12
References

11 May 2010; accepted 21 June 2010
Published online 1 July 2010;
10.1126/science.1192160
Include this information when citing this paper.

Calcareous Nannoplankton Response to Surface-Water Acidification Around Oceanic Anoxic Event 1a

Elisabetta Erba,[1]* Cinzia Bottini,[1] Helmut J. Weissert,[2] Christina E. Keller[2]

Ocean acidification induced by atmospheric CO_2 may be a major threat to marine ecosystems, particularly to calcareous nannoplankton. We show that, during the Aptian (~120 million years ago) Oceanic Anoxic Event 1a, which resulted from a massive addition of volcanic CO_2, the morphological features of calcareous nannofossils traced the biological response to acidified surface waters. We observe the demise of heavily calcified nannoconids and reduced calcite paleofluxes at the beginning of a pre-anoxia calcification crisis. Ephemeral coccolith dwarfism and malformation represent species-specific adjustments to survive lower pH, whereas later, abundance peaks indicate intermittent alkalinity recovery. Deepwater acidification occurred with a delay of 25,000 to 30,000 years. After the dissolution climax, nannoplankton and carbonate recovery developed over ~160,000 years under persisting global dysoxia-anoxia.

The dissolution of an atmospheric CO_2 surplus [that is, over 500 parts per million (ppm)] in the ocean lowers pH and reduces the $CaCO_3$ saturation state, consequently accelerating carbonate dissolution in the deep sea (*1*). The effect of modern surface-water acidification on organisms with $CaCO_3$-based skeletons or tests, such as calcareous nannoplankton, remains elusive (*2*–*6*). Throughout Earth's history, there is evidence of large CO_2 releases, greenhouse conditions, ocean acidification, and major changes in biota, particularly in marine calcifiers (*7*). In many cases, the geological record indicates that ocean biota can adapt to increased acidity; however, past examples of ocean acidification occurred over tens of thousands of years, giving time for life to adjust to CO_2 concentrations as high as 2000 to 3000 ppm (*7*).

The early Aptian [121 to 118 million years ago (Ma)] represents a case history of excess CO_2 derived from a major volcanic episode, namely the emplacement of the Ontong Java Plateau (OJP) (*8*, *9*), which is marked by changes in the evolutionary rates, species richness, abundance, and calcite production of calcareous nannoplankton (*10*–*12*). These changes occurred during Oceanic Anoxic Event 1a (OAE1a) (~120 Ma), which was a time of severe global warming (*13*, *14*). Although global anoxia and enhanced organic matter burial are the most striking and intriguing paleoceanograhic phenomena during this event, OAE1a sediments reveal a sequence of CO_2 pulses (*15*) and weathering changes (*16*). For example, the cutoff of carbonates during OAE1a is the result of volcanogenic CO_2-related ocean acidification (*7*, *10*, *17*).

We analyzed calcareous nannofossil assemblages from two drill sites in the Tethys (Cismon core) and Pacific [Deep Sea Drilling Project (DSDP) site 463] Oceans (fig. S1) (*18*). At both sites, nannofossil changes integrated with geochemical and cyclochronological data (*15*, *19*) identify and date the effects of acidification on calcareous nannoplankton. Shortly before magnetic chron M0 (Fig. 1), at 121.3 Ma (*19*), nannoconid abundance declined and nannofossil paleofluxes (tracing nannoplankton carbonate production and accumulation) decreased as response to a major injection of volcanogenic CO_2. Later, a sharp nannoconid crisis at 120.25 Ma was part of a global calcification failure of planktonic and benthic calcifiers in pelagic and neritic settings under excess CO_2 in the ocean-atmosphere system (*17*). During the 1-million-year-long interval between these two events, the geological record reveals subtle effects of ocean acidification traced only by nannofossils, and specifically by the heavily calcified nannoconids, with trivial effects on other coccoliths and apparently no evidence in the lithologic and geochemical records. Although the negative carbon isotopic event (CIE) at the beginning of global anoxia (~120 Ma) coincides with the drop in carbonate content, there was an increase in relative abundance of *Biscutum constans*, *Zeugrhabdotus erectus*, and *Discorhabdus rotatorius*, represented by dwarfed specimens (Fig. 1). Size variation was species-specific at both sites, because *B. constans* displays the most pronounced morphometric decrease (a volume/mass reduction of 50 to 60% for single coccoliths), whereas *Z. erectus* diminishes in size to a lesser extent (a volume/mass reduction of 30 to 40% for single coccoliths). *D. rotatorius* also exhibits smaller-than-normal sizes throughout the

[1]Dipartimento di Scienze della Terra "Ardito Desio," Università degli Studi di Milano, via Mangiagalli 34, 20133 Milano, Italy. [2]Department of Earth Sciences, Geology, Eidgenössische Technische Hochschule (ETH)–Zentrum, Sonneggstrasse 5, CH-8092 Zürich, Switzerland.

*To whom correspondence should be addressed. E-mail: elisabetta.erba@unimi.it